Fluid dynamics and heat transfer in the wake of a sphere

I. Rodriguez[a,*], O. Lehmkuhl[b], M. Soria[a], S. Gómez[b], M. Domínguez-Pumar[c], L. Kowalski[c]

[a] *Turbulence and Aerodynamics Research Group (TUAREG). Universitat Politècnica de Catalunya-BarcelonaTech. Colom 11, 08222. Terrassa(Barcelona). Spain.*
[b] *Barcelona Supercomputing Centre (BSC). Edificio NEXUS II - Jordi Girona 29 08034 Barcelona, Spain*
[c] *Departamento de Ingeniería Electrónica (DEE) Grupo Micro y NanoTecnología (MNT). Universitat Politècnica de Catalunya-BarcelonaTech Campus Nord, edificio C4, oficina 213 Jordi Girona 1-3, 08034 Barcelona, Spain.*

Abstract

Direct numerical simulation and large-eddy simulation have been performed for a heated sphere at Reynolds numbers of $Re = 1000$ and $Re = 10^4$, respectively. The Prandtl number for both simulations has been $Pr = 0.7$. Measurements of the local and average Nusselt number are performed and compared with literature available experimental results. Average and front stagnation point Nusselt numbers increase with the Reynolds number, while the minimum value moves towards the sphere apex as the flow enters the sub-critical regime. Differences in both viscous and thermal boundary layers are observed, while the shape factor at Reynolds number $Re = 10^4$ behaves similarly to that observed in circular cylinders at comparable Reynolds numbers. It is shown that as the Reynolds number increases, the increase in turbulent kinetic energy promotes the entrainment of irrotational flow thus enhancing the temperature mixing in the zone. The near wake, between $5 \leqslant x/D \leqslant 15$, spreads at a faster rate at $Re = 1000$ with a slope close to $x/D^{1/2}$, while at $Re = 10^4$ it follows a trend close to $x/D^{1/3}$.

*Corresponding author
Email addresses: ivette.rodriguez@upc.edu (I. Rodriguez), oriol.lehmkuhl@bsc.es (O. Lehmkuhl), manel.soria@upc.edu (M. Soria), samuel.gomez@bsc.es (S. Gómez), manuel.dominguez@upc.edu (M. Domínguez-Pumar), lukasz.kowalski@upc.edu (L. Kowalski)

Keywords: axisymmetric wakes, sphere, heat transfer, LES, DNS

1. Introduction

The knowledge about fluid dynamics and heat transfer from spherical bluff bodies is of key importance in many engineering applications and science such as dispersed particle-laden, sprays, pulverized coal combustion, etc. For Reynolds numbers larger than 300 ($Re = 300$) and up to $Re = 800$, the flow is dominated by the laminar shedding of vortices. For larger Reynolds numbers, i.e. in the subcritical regime at $Re < 3 \times 10^5$, a Kelvin-Helmholtz instability is responsible for the inception of small-scale structures in the separated shear layer and the transition from laminar to turbulent flow in the wake. The turbulent wake and the unsteady shedding of vortices from a sphere have been subject of many experimental investigations (see for instance [1, 2, 3, 4]) and in less extent by numerical simulations (e.g. [5, 6, 7] and citations therein). Moreover, at low-to-moderate Reynolds numbers the flow characteristics are dominated by a low-frequency mechanism that alters the way vortices are shed and thus, the wake dynamics [5]. This phenomenon may be important in the case of thermal sensors, if the frequency is within the bandwidth of the thermal filter associated to the structure of the sensor [8].

The self-preserving axisymmetric wake behind a sphere was studied by Uberoi & Freymuth [9] at $Re = 8600$. Later, the same authors studied the self-similarity of the temperature and its fluctuations in the far wake of a sphere at $Re = 4300$ [10]. Wu & Faeth [4] conducted measurements of the wake of a sphere up to $Re = 4000$ and found three regions, a fast decay region followed by turbulent and laminar regions with wake growth $\sim x^{1/3}$ and $\sim x^{1/2}$, respectively. Johansson & George [11] studied the far axisymmetric wake behind a disk and found that similarity equilibrium theory holds for $x/D > 30$. Nedić et al.[12] showed that for axisymmetric wakes behind regular bodies equilibrium theory applies, whereas for wakes behind irregular plates velocity deficit decay and wake width non-equilibrium scaling with exponents of 1 and 1/2 are observed.

This subject was also addressed by de Stadler et al. [13] who performed large-eddy simulations (LES) of the scalar mixing in the turbulent wake of a sphere at $Re = 10^4$ and showed the presence of different scaling rates in the near wake after the recirculation region and in the intermediate wake, $15 \leqslant x/D < 35$. More recently, Dairay et al. [14] performed measurements and simulations of the axisymmetric wake behind irregular plates and presented a revised theory for non-equilibrium axisymmetric wakes. In particular they found that in the range $x/L_b = 10 - 50$ the velocity deficit decays with exponent -0.94, whereas in the range $x/L_b = 55 - 100$ it decays as -0.86. Later, Obligado et al. [15] from the analysis of the experimental and direct numerical simulation (DNS) data, and considering axisymmetry, self-similarity and non-equilibrium dissipation, sustained that the non-equilibrium scaling proposed by Nedić et al. [12] might be universal.

Many experimental and numerical studies have been devoted to the heat (or mass) transfer from a sphere. Most of them have been focused on the measure of the overall Nusselt number on the sphere over a range of Reynolds numbers and the determination of a heat transfer correlation. Among them, Kramers [16] measured heat transfer coefficients for Reynolds numbers from 2.65 to 1460 and Prandtl numbers from 0.741 (air) to 380 (hot oil). He also discussed about the inadequacy of potential flow for theoretical predictions of heat transfer from spheres and cylinders. Yuge[17] performed measurements, not only on forced convection configurations but also including the effect of buoyancy in the experiments, for Grashof numbers from 1 to 10^5 and Reynolds numbers in the range between 3.5 and 1.44×10^5. For the forced convection correlations, he divided the correlations into two ranges with $Re = 1800$ as the point where the slope of the correlations changed. Later, Vliet and Leppert[18] carried out an experimental study with water, for Reynolds numbers in the range between 940 and 5×10^4, considering the effect of the variation of water properties and natural convection. Galloway and Sage [19] reviewed previous works measuring Nusselt and Sherwood numbers and highlighted the importance of turbulence level and sphere diameter. Raithby and Eckert [20] measured Nusselt numbers

for Reynolds numbers in the range between 3600 and 5.2×10^4, in air. They also discussed the effects of the turbulence intensity, sphere supporting device (position and size) and heat losses on the average Nusselt number measured. Using measurements from Vliet and Leppert[18], Yuge[17] and Kramers [16], Whitaker [21] reported a single correlation which is quite well-known and used in many textbooks. Kowalski and Mitchel [22] studied the heat transfer from a sphere in naturally turbulent outdoor environment, finding an increase by a factor up to 2.2 times of the values obtained in low turbulence wind tunnels. Kurose et al. [23] performed numerical simulations of the flow past a heated / cooled sphere, considering the buoyancy effects and large temperature differences between the fluid and the sphere, for Reynolds numbers in the range between 50 and 500. They pointed out the strong dependence of the thermophysical properties on the temperature and thus, the inapplicability of the Boussinesq approximation as the temperature gradient increases. More recently, Will et al. [24] carried out an experimental study with air and Reynolds numbers in the range between 7800 and 3.3×10^5. They observed a sudden increase in the overall Nusselt number, analogous to the drag crisis, for a critical Reynolds number of approximately 2.9×10^5.

Despite the large number of experiments performed on spheres for measuring the overall heat transfer coefficient, the study of the local coefficient has received lesser attention. Short et al. [25] measured local Nusselt numbers for Reynolds numbers up to 3600 in an airstream at several apparent turbulence levels. They observed that although the turbulence intensity does increase the Nusselt number, at low levels of turbulence in the front stagnation point the Nusselt number decreases to increase again as the turbulence intensity increases. From their measurements, they also extrapolated the values of the non-dimensional heat transfer coefficient at zero turbulence level. Lee and Barrow [26] calculated the development of diffusion from the forward stagnation point with boundary layer equations, and measured local Sherwood numbers for several Reynolds numbers (3199 to 2.5×10^4) using a method based on naphthalene sublimation. Zhitkevich and Simchenko [27] measured local Nusselt numbers for Reynolds numbers

in the range from 50 to 9.7×10^5 and Galloway and Sage [28] for Reynolds numbers in the range from 5.200 to 7.02×10^4 and several turbulence levels. Hayward and Pei [29] measured local Nusselt numbers for $Re = 2600 - 6100$ and several turbulence levels. They observed the decrease of the Nusselt number towards the boundary layer separation and a sudden increase in the back of the sphere which was attributed to the formation of a recirculation bubble in this zone. The numerical studies of the local heat transfer are even more scarce. Among them, the direct numerical simulations performed by Bachgi et al. [30] at Reynolds numbers up to 500. They observed that the shedding process in the range studied was asymmetric with the consequent loss of symmetry in the surface heat transfer.

There is a large scattering in the measurements of the Nusselt number mainly due to the effects of the turbulence intensity and length scale, as well as the effects of the support mechanism of the sphere that makes the obtention of accurate measurements a very challenging task. Moreover, most of the studies performed so far have been focused on heat transfer measurements but few studies can be found about the boundary layer development and its role on the wake development from heated spheres. The present work is motivated for the development of a spherical wind sensor for Mars atmosphere[31], intended for future missions after Rover 2020. Thus, the analysis of the thermal interaction of the sphere with the wind for Mars atmosphere is a key aspect of its design, although other applications for Earth atmosphere can also been considered. The present work aims to analyse the boundary layer development and heat transfer, together with the near wake behaviour for a sphere at the moderate Reynolds numbers of $Re = 1000$ and $Re = 10^4$ and Prandtl number $Pr = 0.7$. The lower Reynolds number is related to extreme conditions in Mars, such as dust devil, whereas the larger Reynolds number corresponds with Earth atmosphere applications. The remainder of this paper is organised as follows. First, the mathematical and numerical models used, together with the definition of the problem are presented in Section 2. In Section 3, details of the dynamics of the flow and heat transfer from the sphere are discussed, together with the boundary

layer development and the behaviour of the flow in the near wake. Conclusions are drawn in Section 4.

2. Mathematical and numerical methods

The incompressible Navier-Stokes and energy equations can be written as

$$\frac{\partial u_i}{\partial x_i} = 0 \tag{1}$$

$$\frac{\partial u_i}{\partial t} + \frac{\partial u_i u_j}{\partial x_j} - \nu \frac{\partial^2 u_i}{\partial x_j \partial x_j} + \rho^{-1} \frac{\partial p}{\partial x_i} = 0 \tag{2}$$

$$\frac{\partial T}{\partial t} + \frac{\partial u_j T}{\partial x_j} - \kappa \frac{\partial^2 T}{\partial x_j \partial x_j} = 0 \tag{3}$$

where x_i are the spatial coordinates (or x, y, and z), u_i (or u, v, and w) stands for the velocity components and p and T are the pressure and temperature fields; ν is the kinematic viscosity, ρ the density of the fluid and κ is its thermal diffusivity.

By spatially filtering the above equations, the LES equations can be obtained,

$$\frac{\partial \overline{u}_i}{\partial x_i} = 0 \tag{4}$$

$$\frac{\partial \overline{u}_i}{\partial t} + \frac{\partial \overline{u}_i \overline{u}_j}{\partial x_j} - \nu \frac{\partial^2 \overline{u}_i}{\partial x_j \partial x_j} + \rho^{-1} \frac{\partial \overline{p}}{\partial x_i} = -\frac{\partial \mathcal{T}_{ij}}{\partial x_j} \tag{5}$$

$$\frac{\partial \overline{T}}{\partial t} + \frac{\partial \overline{u}_j \overline{T}}{\partial x_j} - \kappa \frac{\partial^2 \overline{T}}{\partial x_j \partial x_j} = -\frac{\partial \mathcal{T}_{Tj}}{\partial x_j} \tag{6}$$

where $(\overline{\cdot})$ stands for the filtered variables. The terms $\mathcal{T}_{ij}$ and $\mathcal{T}_{Tj}$, the subgrid stresses and subgrid-scale heat fluxes, in equations 5 and 6 are resulting from the filtering of the non-linear terms and must be modelled. The anisotropic part of the subgrid stress tensor (SGS) is given as,

$$\mathcal{T}_{ij} - \frac{1}{3}\mathcal{T}_{kk}\delta_{ij} = -2\nu_{sgs}\overline{\mathcal{S}}_{ij} \tag{7}$$

where $\overline{\mathcal{S}}_{ij} = \frac{1}{2}(g_{ij} + g_{ji})$ is the large-scale rate-of-strain tensor, and $g_{ij} = \partial\overline{u}_i/\partial x_j$; δ_{ij} is the Kronecker delta. Here the term $\overline{p}$ in equation 5 is a modified filtered pressure that includes a term proportional to the turbulent kinetic energy ($k = \frac{1}{2}\overline{u_i u_i}$), $\overline{p} = \hat{p} + \frac{2}{3}\rho k$ and $\hat{p}$ is the actual filtered pressure. The formulation is closed by an appropriate expression for the subgrid-scale viscosity, ν_{sgs}. In this work, the model proposed by Vreman [32] is used. This model is constructed in such a way that it is suitable for unstructured grids and has good properties such as, it is rotationally invariant for isotropic filter widths, vanishes at the walls or in two-dimensional flows, and its dissipation is relatively small in transitional flows. Regarding the turbulent scalar flux, the gradient-diffusion hypothesis is used: $\mathcal{T}_{Tj} = \kappa_{sgs}\frac{\partial T}{\partial x_j}$, with $\kappa_{sgs} = \nu_{sgs}/Pr_t$; Pr_t is the turbulent Prandtl number. Here, $Pr_t = 0.7$ is assumed.

The above equations are solved by means of a low-dissipation finite element (FE) scheme [33]. The basic idea behind this approach is to mimic the fundamental symmetry properties of the underlying differential operators, i.e., the convective operator is approximated by a skew-symmetric matrix and the diffusive operator by a symmetric, positive-definite matrix. The chosen low dissipation FE scheme presents good accuracy compared to other low dissipation finite volume and finite difference methods, with the advantage of being able to increase the order of accuracy at will without breaking the fundamental symmetry properties of the discrete operators. A non-incremental fractional-step method is used to stabilise the pressure. This allows for the use of finite element pairs that do not satisfy the inf-sup conditions, such as the equal order interpolation for the velocity and pressure used in this work. The set of equations is time integrated using an energy conserving Runge-Kutta explicit method lately proposed by Cappuano et al. [34], combined with an eigenvalue based time-step estimator [35]. This methodology is implemented into the code Alya, which is a multi-physics parallel code organized in a modular way: kernel, services and modules, which can be separately compiled and linked. Each module represents a single set of Partial Differential Equations (PDE) for a given physical model. To solve a coupled multi-physics problem, all the required modules must be

active and interacting following a well-defined workflow. For more details, the reader is referred to [36].

2.1. Definition of the cases and boundary conditions

The fluid dynamics and heat transfer around a heated sphere at Reynolds numbers $Re = 1000\,, 10^4$ and Prandtl number $Pr = \nu/\kappa = 0.7$ are considered. Here, the Reynolds number $Re = U\,D/\nu$ is defined in terms of the free-stream velocity U and the sphere diameter D. The thermo-physical properties are set so as to obtain the desired Reynolds and Prandtl numbers. At $Re = 1000$, a direct numerical simulation (DNS) has been performed, whereas at $Re = 10^4$ the flow has been solved by means of large-eddy simulations (LES).

The cases are solved in a cylindrical computational domain of dimensions $x \equiv [-5.5D : 25.5D]$; $r \equiv [0, 10D]$; $\phi \equiv [0, 2\pi]$ with the sphere located at $(0, 0, 0)$. This domain has similar dimensions to that used in the DNS of Rodriguez et al. [5, 6]. The boundary conditions at the inflow consist of uniform velocity and temperature fields $(u/U, v/U, w/U) = (1, 0, 0)$. The temperature can be expressed in non-dimensional form as $\Theta = (T - T_{in})/(T_{sph} - T_{in})$, thus, $\Theta = 0$ has been set at the inlet. T_{sph} and T_{in} are the values of the temperature at the sphere surface and at the inlet, respectively. However, as the velocity and temperature fields are not coupled and the temperature is here treated as a passive scalar, the actual values of T_{sph} and T_{in} are irrelevant to the problem studied. At the outlet, a pressure-based condition has been used, i.e. $p - 0.5\gamma\rho\,u_n^2 = 0$ with u_n being the normal velocity at the outlet boundary and γ an expansion coefficient; $\gamma = 1$ in this work [5]. For the temperature at the outlet, $\partial\Theta/\partial n = 0$ has been set. At the sphere surface, a no-slip boundary condition for the velocities has been imposed and a Dirichlet condition for the temperature, $\Theta = 1$, has been prescribed. At the lateral boundary of the domain, the derivative of the tangential velocity components and the normal velocity are set to zero, while a Neumann condition ($\partial\Theta/\partial n = 0$) for the temperature is used.

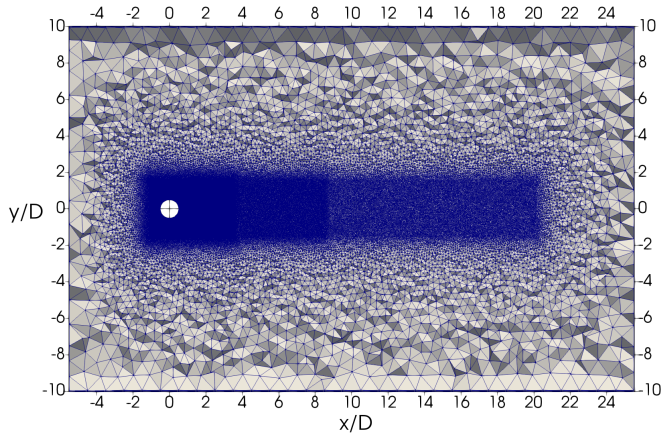

Figure 1: Projection of the central plane of the computational domain. The mesh distribution with the different zones in the domain can be observed. The sphere is located at (0,0,0).

2.2. Grid sensitivity study

The computational meshes have been designed as follows. Three inner cylindrical regions of radius 1.5D, extended in the stream-wise direction up to $x/D = 3.5$, 8.5, 20 from the sphere center have been generated. The sizes of the elements at these zones are given in Table 1 and are denoted as Δ_{z1}, Δ_{z2} and Δ_{z3}, respectively. The size of the outer/external zone Δ_{z4} is also given in the table. To generate the mesh, first the superficial mesh with element size of Δ_{sph} (see Table 1) is generated. A view of the central plane of the domain, where the different zones can be seen, is shown in figure 1. The meshes considered in this work are designed so as to solve well the boundary layer around the sphere. At these Reynolds numbers, the boundary layer that develops at the sphere surface is laminar (the transition to turbulence in the boundary layer occurs at $Re \sim 2 \times 10^5$[1]), thus the meshes close to the sphere are calculated following the same criteria used by Tomboulides & Orszag [37] and Rodriguez et al. [6]. With this in mind, in the near wall region the number of elements within the boundary layer for the most demanding case (i.e. $Re = 10^4$) is about 5-12 gridpoints (see Table 1 for more details). Moreover, the non-dimensional wall-normal distance has been kept $y^+ < 2$ for the most demanding case, i.e.

Table 1: Meshes used in the simulation. N_{CVs}, total number of elements, N_{dof} number of degree-of-freedom, Δ_{sph} size of the elements on the surface of the sphere, Δ_{z1} to Δ_{z4} size of the elements in the regions 1 to 4 in the wake of the sphere, N_{BL} number of grid points within the boundary layer (calculated for $Re = 10^4$).

Mesh	N_{CVs}	N_{dof}	Δ_{sph}	Δ_{z1}	Δ_{z2}	Δ_{z3}	Δ_{z4}	N_{BL}
m1	9.6×10^6	1.7×10^6	0.0050	0.050	0.08	0.12	0.75	3-8
m2	3.27×10^7	5.6×10^6	0.0025	0.025	0.05	0.12	0.75	5-12

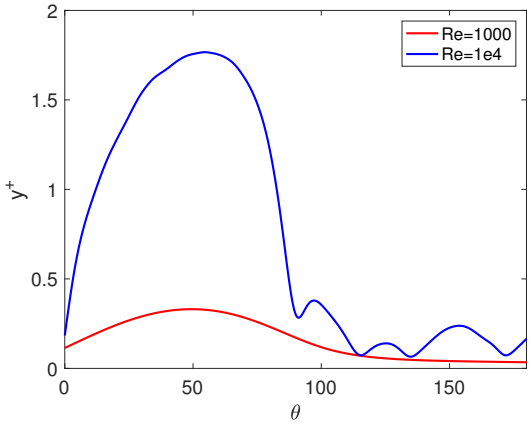

Figure 2: Mesh resolution near the wall for $Re = 1000$ and $Re = 10^4$

$Re = 10^4$. Being $\tau_w = \mu \partial v_\theta / \partial n$, the skin friction defined as the wall normal derivative of the velocity vector at the wall and $u_\tau = \sqrt{(\tau_w/\rho)}$ the friction velocity, the non-dimensional wall normal distance can be defined as $y^+ = u_\tau r/\nu$, with r the wall-normal distance. The non-dimensional wall-normal distance with mesh m2 for both Reynolds numbers is given in figure 2. This resolution is comparable to that used in the DNS of Rodriguez et al. [6] and in the wall resolved LES of Stadler et al. [13]. Note that the largest values of y^+ are attained in the zones where the boundary layer is laminar, i.e. in the front part of the sphere, whereas in the rear zone the values of this quantity are rather small even for the largest Reynolds number.

The results of the simulations obtained with the two computational grids have been compared to those of the literature. At $Re = 1000$, Tomboulides & Orszag [37] performed DNS using a spectral element/Fourier spectral method on a computational mesh of 2.6 million of degree-of-freedom. Moreover, experimental measurements reported by Wu & Faeth [4] have also been used. At $Re = 10^4$, the statistical data have been compared to the DNS results of Rodriguez et al. [6] obtained on a computational mesh of 18.2 million of degree-of-freedom.

In order to obtain the turbulent statistics presented in this paper, the flow has been advanced in time up until statistical stationary flow regime has been reached. After that, statistics have been collected and averaged in time. Figure 3 depicts the drag and both lateral (side) force coefficients (C_y and C_z) on the sphere. These coefficients are the non-dimensional total force F_i on the surface in each direction, $C_i = F_i/(1/2\rho U^2 A_{ref})$ with $i = 1,\ 2,\ 3$ or $x,\ y,\ z$ directions. The drag coefficient C_d corresponds to the streamwise direction x. As can be seen from the time history of the drag and side force coefficients in figure 3, for Re=1000 the statistical stationary state is reached around 100 time units (TU, the non-dimensional time is here defined as $t^* = tU/D$), whereas for $Re = 10^4$ the flow stabilises around 50 TU. Thus, average statistics have been integrated in time for about 300TU and 250TU for $Re = 1000$ and $Re = 10^4$, respectively. Note that these integration times are larger than those used in previous DNS of Tomboulides & Orszag [37] and Rodriguez et al. [6] where statistics were obtained for 130TU and 150TU, respectively.

The results of some of the flow features obtained with the two levels of refinement are shown and compared to previous literature results in Table 2 . In the table, C_d is the mean drag coefficient, and $C_{d,rms}$ its root mean square value; $C_{y,rms}$ and $C_{z,rms}$ are the root mean square values of the y-force and z-force coefficients, respectively; $-C_{pb}$ is the base pressure coefficient (the pressure coefficient at the back of the sphere). The pressure coefficient is defined as $Cp = \frac{p-p_{ref}}{0.5\rho U^2}$, p_{ref} being the reference pressure, the pressure at the inlet in this work. The separation angle θ_{sep} (measured from the front stagnation point) and the non-dimensional vortex shedding-frequency, St (i.e., Strouhal number

Table 2: Mesh sensitiveness study. Flow parameters for Reynolds numbers $Re = 1000$ and $Re = 1 \times 10^4$ and comparison with literature results. Drag coefficient C_d, fluctuating drag $C_{d,rms}$, fluctuating y-force $C_{y,rms}$, fluctuating z-force $C_{z,rms}$, base pressure coefficient $-C_{pb}$, separation angle θ_{sep}, non-dimensional vortex shedding frequency St.

mesh	C_d	$C_{d,rms}$	$C_{y,rms}$	$C_{z,rms}$	$-C_{pb}$	θ_{sep}	St
$Re = 1000$ (DNS)							
m1	0.466	0.0072	0.017	0.016	0.211	101.1	0.178
m2	0.466	0.0076	0.012	0.013	0.213	101.4	0.200
Sakamoto & Haniu [38]	-	-	-	-	-	-	0.200
Tomboulides &Orszag (DNS) [37]	-	-	-	-	-	102.0	0.195
$Re = 10^4$ (LES)							
m1	0.406	0.0093	0.025	0.025	0.298	89.9	0.213
m2	0.402	0.0071	0.022	0.023	0.293	90.0	0.216
Constantinescu et al.[39] (LES)	0.393	-	-	-	0.229	85.0	0.195
Yun et al. [40](LES)	0.393	-	-	-	0.274	90.0	0.170
Rodriguez et al.[6](DNS)	0.402	-	-	-	0.272	84.7	0.195

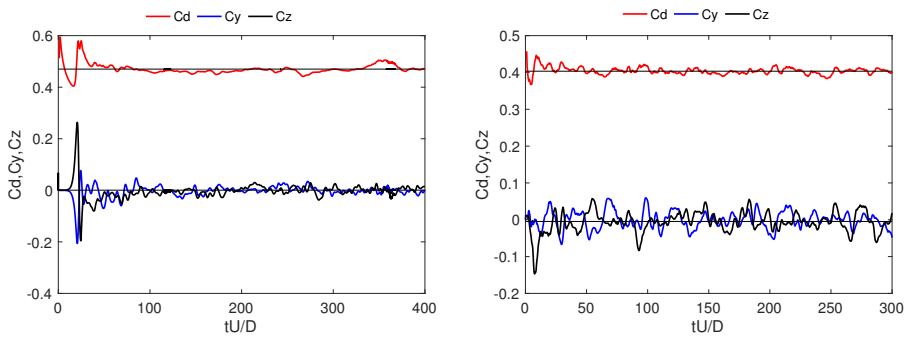

Figure 3: Time history of the drag (C_d), y-force (C_y) and z-force (C_z) coefficients. (a) $Re = 1000$, (b) $Re = 10^4$.

$St = f_{vs}D/U$) are also given in the table. As can be seen, even the coarse mesh reproduces quite well the main flow features for both Reynolds numbers. Moreover, the averaged stream-wise velocity and its fluctuations along the wake centreline are plotted in figure 4. Similarly to the averaged flow coefficients, both meshes are in quite good agreement with the results from the literature, although as expected, m2 gives slightly better results. Note that for $Re = 1000$, even though the location of the maximum peak of the velocity fluctuations in the wake centreline is in agreement with the results reported by Tomboulides et al.[37], there is a difference in the magnitude of the peak. These differences might be attributed to the integration time, the mesh density used in the zone or the numerical schemes, among other causes. However, as the differences between the meshes m1 and m2 are small, we assume that the results obtained with m2 are mesh converged. In what follows, all the results presented for both Reynolds numbers are given with mesh m2.

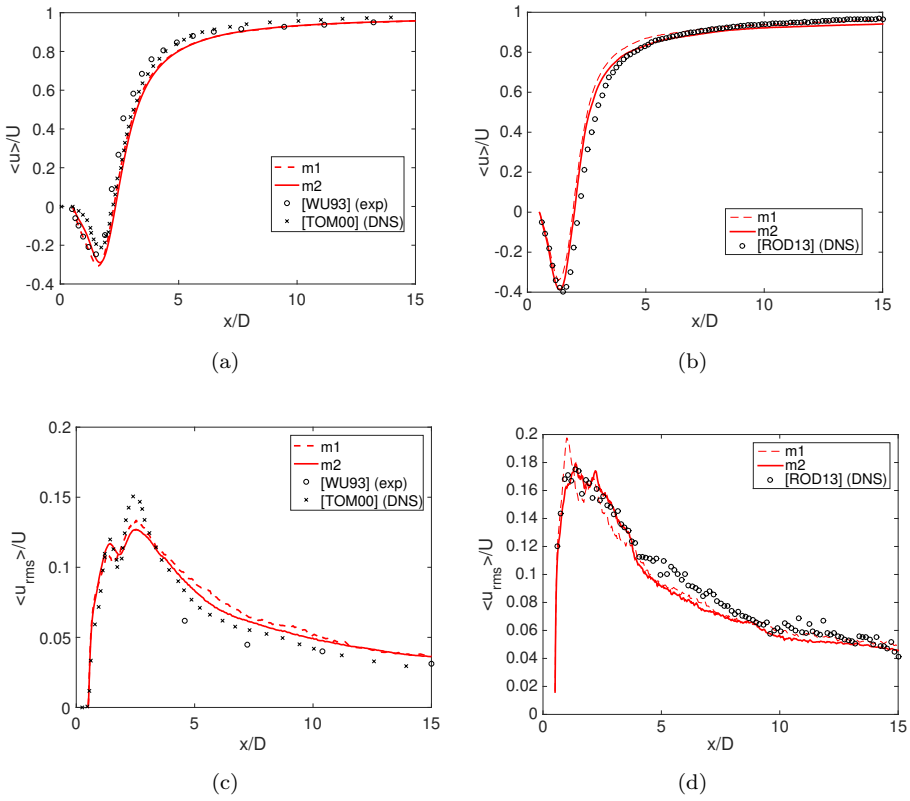

Figure 4: Mesh sensitiveness study. Stream-wise velocity in the wake centreline at (a) $Re = 1000$ and (b) $Re = 10^4$. Fluctuation of the stream-wise velocity in the wake centreline at (c) $Re = 1000$ and (d)$Re = 10^4$. Comparison with results from the literature [WU93] Wu & Faeth [4], [TOM00] Tomboulides & Orszag [37], [ROD13] Rodriguez et al. [6].

3. Results

3.1. Fluid flow

In the range of Reynolds numbers concerning the present paper, significative changes in the wake of the sphere occur. It has been reported in the literature that beyond $Re = 800$ a secondary instability appears in the separated shear layer, called Kelvin-Helmholtz (KH) instability, which usually presents larger frequencies than those of the vortex shedding [41]. Above $Re = 800$, the flow becomes unstable giving raise to a turbulent wake, while separation from the sphere is still laminar. This range of Reynolds numbers, in which separation is laminar but transition to turbulence occurs in the wake is also referred to as sub-critical regime, and extends up to $Re \approx 2.3 \times 10^5$ [42]. The main characteristics of the flow (e.g. drag coefficient, non-dimensional vortex-shedding frequency, separation from the sphere) in the subcritical range of Reynolds numbers remains more or less constant, but at the lower part of this regime there are still differences [41]. Actually, these flow parameters stabilize around $Re = 6000 - 10^4$, once the wake has fully transitioned to a turbulent regime [2, 41]. In the intermediate range, between $Re = 800$ and $Re = 6000$, the wake is still in transition from a laminar to a turbulent regime and some of the characteristics reported along the sub-critical regime (e.g. vortex shedding frequency, drag coefficient, boundary layer separation point, etc.) are not yet observed. Regarding the heat transfer, there are more uncertainties about how these changes in the flow affect the Nusselt number. For instance, some authors found more appropriate to define two equations with a change in slope at around $Re = 1700 - 1800$ [17, 20] instead of one equation to correlate the Nusselt number for the whole range.

The vortical structures at both Reynolds numbers $Re = 1000$ and $Re = 10^4$ are shown in figures 5 and 6, respectively. These structures are represented by means of iso-countours of the second-invariant of the velocity gradient tensor Q[43]. According to the Q criterion, a vortical structure is identified in a region with positive Q, i.e. a region where vorticity overcomes the strain. In both

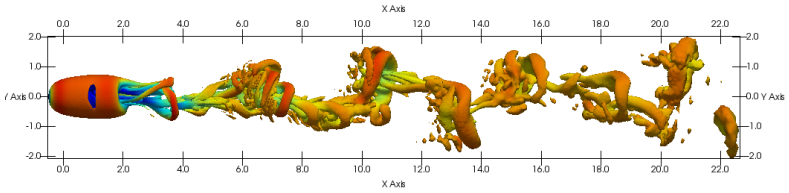

(a)

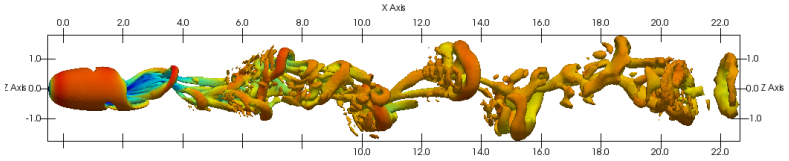

(b)

Figure 5: Coherent structures. Instantaneous Q*=0.02 iso-surfaces at Re=1000. (a) Lateral view, (b) Bottom view.

figures, the wake is represented by two perpendicular views, i.e. front and bottom views. Note also the change in the value for the Q-iso-surfaces, which is lower at $Re = 1000$ as at this Reynolds number vortical structures are quasi-laminar and thus, correspond with low values of Q.

At the lowest Reynolds number, $Re = 1000$, the hairpin-like structures detached from the sphere form regular vortices that move downstream in a helical-like manner as discussed in Rodriguez et al. [5]. The large scale vortices shed from the sphere break into small-scale structures forming a turbulent wake at $Re = 10^4$. Note also the KH like structures in the laminar part of the shear layer. These instabilities are responsible for triggering the transition to turbulence in the wake (see for instance figure 6). Their footprint can also be observed inspecting the energy spectrum of the velocity fluctuations of a numerical probe located in the shear layer. In figure 7, the energy spectrum of the cross stream velocity fluctuations (v') is depicted for probes placed at two different locations, one in the separated shear layer at $(x/D, r/D) \equiv (1.0, 0.6)$ and the second one, in the wake of the sphere at $(x/D, r/D) \equiv (2.0, 0.6)$. For

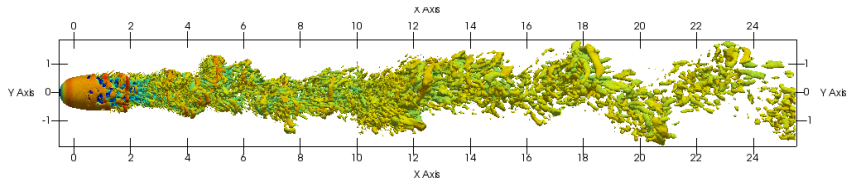

(a)

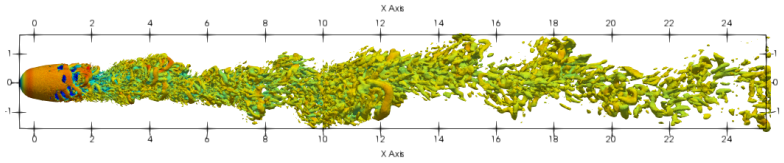

(b)

Figure 6: Coherent structures. Instantaneous Q*=0.4 iso-surfaces at $Re10^4$ (a) Lateral view, (b) Bottom view.

convenience, at each of these locations eight azimuthally equispaced probes are set and their spectrum azimuthally-averaged. In the figure, the DNS spectra at $Re = 10^4$ are also plotted for comparison. As can be seen from the spectrum of the probe located in the separated shear layer (see figure 7a,c), the KH instabilities are observed as a broadband frequency peak. At $Re = 1000$, this peak is centered at $f_{KH}D/U = 0.31$, which is in good agreement with the experimental values reported in the literature $f_{KH}D/U = 0.31 - 0.32$ [3, 38]. As expected, as this frequency is associated with the instability of the shear layer, it increases with the Reynolds number. Thus, at $Re = 10^4$ this peak is centered at $f_{KH}D/U = 1.75$, which is quite close to the value reported by Rodriguez et al. [6] of $f_{KH}D/U = 1.77$. In addition to the energy spectrum of the shear layer, in figure 7b,d the spectra of the probes located in the wake are plotted. At $Re = 1000$, the spectrum does not follow the $-5/3$ decay. Instead, it exhibits a more pronounced decay similar to what was observed by Rodriguez et al. [5] at $Re = 3700$, as at this location the flow is in transition to turbulence. Further downstream, the $-5/3$ decay is observed (not shown here), but the range of frequencies at which this slope occurs is quite narrow. At this low Reynolds

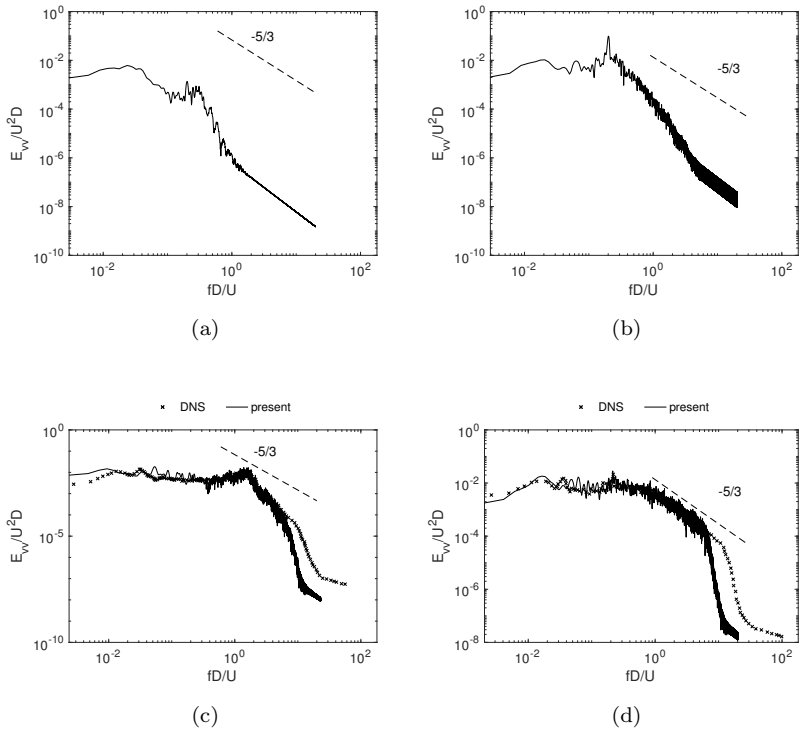

Figure 7: Energy spectrum of the cross-stream velocity fluctuations at different locations (a,c) at $(x/D, r/D) \equiv (1.0, 0.6)$ and (b,d) at $(x/D, r/D) \equiv (2.0, 0.6)$, for Reynolds numbers (a,b) $Re = 1000$ and (c,d) $Re = 10^4$. Comparison with results by Rodriguez et al. [6] at $Re = 10^4$.

number, the energy cascade almost passes from the energy containing scales to the dissipative ones. For the larger Reynolds number, i.e. $Re = 10^4$, the present data match the DNS one over a large range of scales, although as expected at high frequencies it decays early as a result of the LES filtering.

Apart from the differences in the vortical structures shed into the wake, separation from the sphere changes when the Reynolds number increases from 1000 to 10^4. At $Re = 1000$, separation occurs past the apex of the sphere at a location around $\theta_{sep} = 101^\circ$ (see values reported in table 2). When the flow stabilizes around $Re = 3000$, the separation point moves backwards towards the apex and it remains in the same location during the whole sub-critical regime

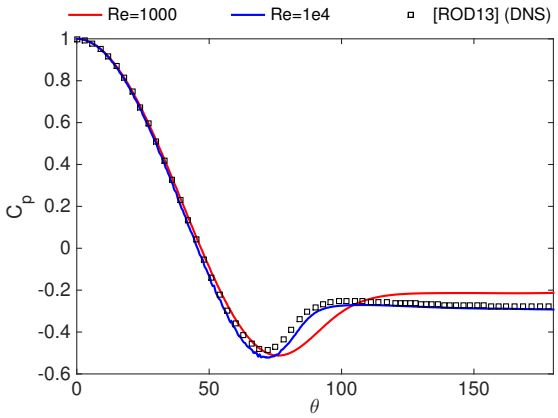

Figure 8: Pressure distribution along the sphere circumference at $Re = 1000$ and $Re = 10^4$. Comparison with DNS results by Rodriguez et al.[6] at $Re = 10^4$.

up until the drag crisis occurs [1].

As the separation point moves backwards, the location of the pressure minimum also moves towards the front stagnation point, while the back pressure gets more negative (see figure 8); as a consequence the drag coefficient also decreases (table 2). With the back pressure reduction, not only the force balance on the sphere changes, but also the entrainment of irrotational flow and the mixing in the near wake become more intensive. This increased mixing can be observed in the temperature field of the near wake in figure 9. Note that the scale of the temperature contours has been conveniently arranged for visualization purposes. Here, the temperature behaves as a passive scalar, i.e. the turbulent field drives the transport of the temperature, but the influence of the temperature field and gradients on the velocity field are neglected. Turbulence induces a rapid mixing and a decay of the temperature with the distance from the sphere in the vortex formation zone. This decay is much faster at $Re = 10^4$, as will be discussed in section 3.4.

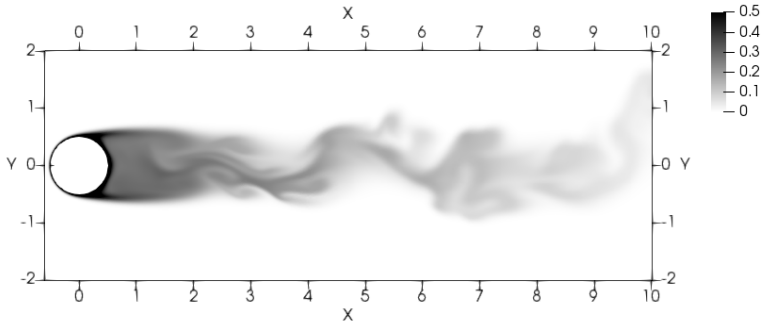

(a)

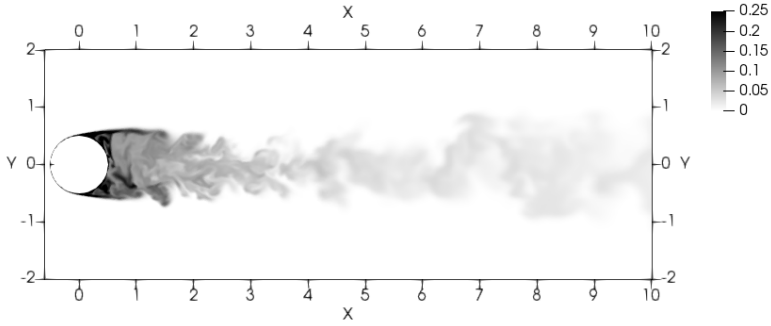

(b)

Figure 9: Temperature field in the wake of the sphere at (a) $Re = 1000$, (b) $Re = 10^4$

Table 3: Surface averaged Nusselt number and its fluctuations. Comparison with literature correlations from Raithby & Eckert[20], Yuge[17] and Withaker[21]. The value of the averaged Nusselt number at the stagnation point $< Nu_{st} >$ is also given.

	$< Nu >$	$< Nu_{rms} >$	$< Nu_{st} >$
	Re=1000		
present DNS	17.40	0.14	36.30
Yuge (corr)	17.59		
Whitaker (corr)	18.16		
Raithby & Eckert (corr)	16.17		
	$Re = 10^4$		
present LES	54.93	1.31	106.60
Yuge (corr)	57.30		
Whitaker (corr)	61.58		
Raithby & Eckert (corr)	57.80		

3.2. Average and local Nusselt number.

The Nusselt number at the surface of the sphere is defined as $Nu = h\,D/k$, where k is the thermal conductivity and h the local dimensional convective heat transfer coefficient defined as:

$$h = \frac{k\partial < T > /\partial n}{(T_{sph} - T_{in})D} = k\frac{\partial \Theta}{\partial n} \tag{8}$$

where $< \cdot >$ stands for the average in time fields. Surface average Nusselt number and its fluctuations are given for both Reynolds numbers in Table 3. Reference values obtained from correlations reported in the literature are also included. In general, the agreement of the average Nusselt number with those reported in the literature is quite good, although for the larger Reynolds number the value obtained is lower than those reported experimentally. Yet, among the different references there are also some discrepancies. Actually, there are different issues that can affect the experimental measurements, especially those of the heat transfer coefficient. Among these, the support mechanism and its

relative position respect the main stream, the turbulence intensity, the scale of turbulence and the heat losses through the support can be found. Raithby and Eckert [20] analysed some of these aspects and found that placing the stem crossflow results in an increase of the Nusselt number in 10% respect at its position in the rear end of the sphere. Similarly, they detected that 5% increase in the turbulence intensity might represent an increase in the Nusselt number by 7.5% and 17.5%, for Reynolds numbers 3.6×10^3 to 5.2×10^4, respectively.

The local Nusselt number for both Reynolds numbers is shown in figure 10. In figure 10, both instantaneous and time-average distribution are given. Note that in order to project the surface of the sphere onto a 2D plane, a normal cylindrical projection is used. In the center of this projection, i.e. $[\phi, \psi] \equiv [0, 0]$, the front stagnation point is located, whereas the lines $[\phi, \psi] \equiv [\phi, \pm 90^\circ]$ correspond to single points in the spherical coordinates. In the figure, the white lines indicate the location of the boundary layer separation. Complementing these contours, plots of the time-average Nusselt number as a function of the angle θ, measured from the front stagnation point and the skin-friction distribution are given in figures 11 and 12, respectively.

As at both Reynolds numbers the attached boundary layer is laminar, the local and time-average Nusselt number distribution in the front of the sphere is almost the same. Fluctuations in this zone are rather small up until the flow approaches the line corresponding with the flow separation. In the front stagnation point, the largest value of the Nusselt number is attained (see also values reported in table 3). Then, it decreases up to a minimum which occurs just after the boundary layer separation point (see figures 11 and 12, and also the separation location reported in table 2). This minimum value is attained at $\theta \approx 114^\circ$ and $\theta \approx 95^\circ$ for Re=1000 and $Re = 10^4$, respectively. After separation, the Nusselt number increases moderately towards the rear stagnation point. Note also that at $Re = 10^4$ the transition to turbulence in the wake is closer to the surface of the sphere than at Re=1000, therefore, there is more mixing in the aft region of the sphere as can be observed in the instantaneous plots in figure 10f,h.

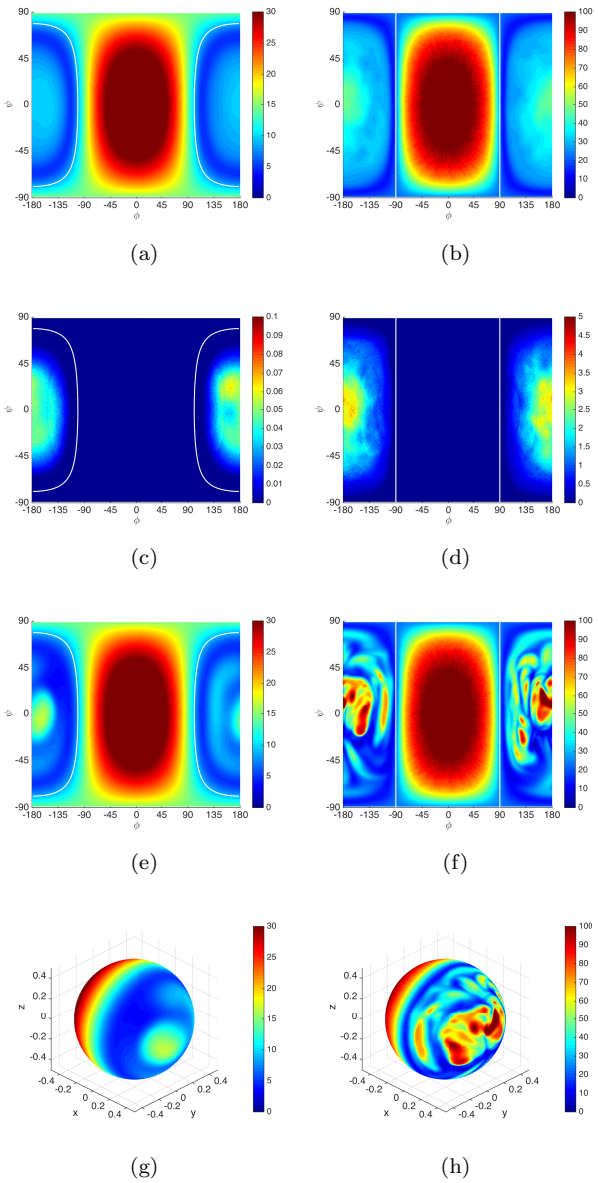

Figure 10: Local Nusselt number at (a,c,e,g) $Re = 1000$ and (b,d,f,h) at $Re = 10^4$. (a,b) time average Nusselt number, (c,d) Nusselt number fluctuations Nu_{rms}, (e,f) typical instantaneous Nusselt number, (g,h) 3D view of the instantaneous Nusselt number.

Respect to the fluctuations of the Nusselt number distribution (Nu_{rms}), it is worth mentioning its relation with the budget for Θ'^2 [44]. At the wall, the scalar-dissipation can be expressed as $2\kappa N u_{rms}^2$. Since non-slip $u_i = 0$ and constant temperature $\Theta = 1$ are imposed, the mean substantial derivative of Θ'^2, the scalar-variance production term and convective part of the flux term vanish. Hence, the scalar-dissipation is in equilibrium with the diffusive transport of scalar variance. However, before the boundary layer separation occurs both are very low due to the laminar inlet assumption, as can be seen in figure 10 (e,f), while the higher values concentrate at the rear stagnation point.

A close comparison of the local Nusselt number along the sphere circumference with the values reported in the literature is given in figure 11. For comparison purposes, the Nusselt number has been scaled as $Nu\ Re^{-0.5}$ following the analytical solution for the laminar boundary layer for bodies of revolution proposed by Frössling [45]. In the figure, both Reynolds numbers have been presented independently as the flow dynamics and the heat transfer vary when the Reynolds number increases from $Re = 1000$ to $Re = 10^4$ (see section 3.1). Although the agreement is rather good, there are some differences with the experimental data that can be attributed to the same issues discussed above (i.e. free-stream turbulence, location of the support, etc.). However, the deviation with the experimental data by Hayward & Pei [29] can not be attributed to the effects of the turbulent stream in the measurements, as the deviations in the front of the sphere are too large to be due to free-stream turbulence [20]. On the other hand, it could be attributed to the location of the stem, but in their paper there were no details about the sphere support. For both Reynolds numbers, the distributions obtained in the laminar boundary layer zone perfectly match with the extrapolated values at zero turbulence intensity reported by Short et al.[25]. A significant difference between the two Reynolds numbers is that for $Re = 1000$, the decrease of the Nusselt number from the stagnation point to the location of the minimum occurs more or less at a constant rate. However, for $Re = 10^4$, this behaviour is different with a mild decrease in the Nusselt number up to an angular position $\theta \approx 65^\circ$ to sharply decrease towards the separation

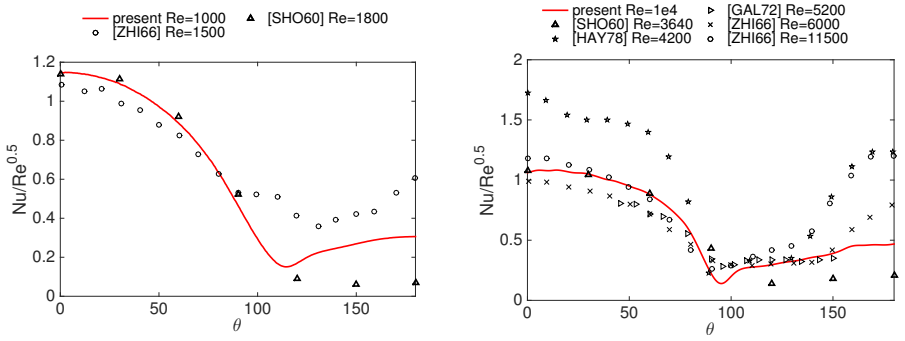

(a) (b)

Figure 11: Distribution of the Nusselt number along the sphere circumference at (a) Re = 1000, (b) $Re = 10^4$. Comparison with the literature. [SHO60] Short et al.[25], [ZHI66] Zhitkevic & Simchenko[27], [GAL72] Galloway & Sage [28], [HAY78] Hayward & Pei [29]

line.

3.3. Boundary layer development

The viscous and thermal boundary layer thicknesses and the shape factor for both Reynolds numbers are given in figure 13. Here, the viscous boundary layer thickness (δ_{95}) is defined as the location where the velocity is the 95% of the velocity at the outer edge of the boundary layer. In a similar manner, the thermal boundary layer thickness δ_Θ is defined as the location where the non-dimensional temperature is 5% above the temperature of the free-stream, i.e. $\Theta = 0$. The shape factor, $H = \delta_1/\delta_2$, is the ratio of the displacement, δ_1, to the momentum thicknesses, δ_2. These quantities are defined as,

$$\delta_1 = \int_0^{\delta_{95}} \left(1 - \frac{v_\theta}{U_e}\right) dn; \quad \delta_2 = \int_0^{\delta_{95}} \frac{v_\theta}{U_e}\left(1 - \frac{v_\theta}{U_e}\right) dn. \tag{9}$$

where v_θ is the stream-wise velocity in the boundary layer of the sphere, U_e the velocity at the edge of the boundary layer and n the normal direction to the surface of the sphere.

As expected, as the Reynolds number increases the boundary layer becomes

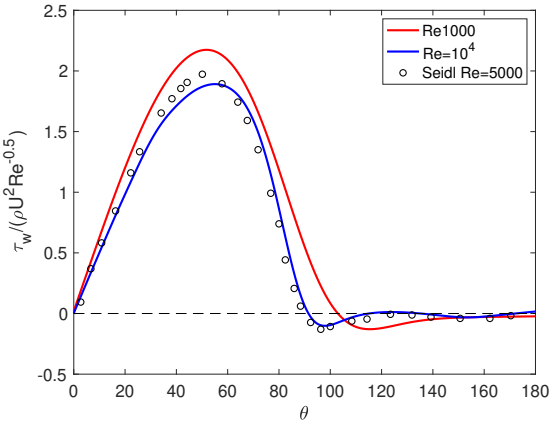

Figure 12: Skin-friction distribution along the sphere circumference at both Reynolds numbers. Comparison with measurements by Seidl et al.[46]

thinner and as $Pr < 1$, the thermal boundary layer is thicker than the viscous one. The shape factor shows a more interesting behaviour. For both Reynolds numbers, at low angles from the front stagnation point, both boundary layers have the same shape factor which is slightly lower than the value predicted by Blasius solution for a laminar boundary layer, $H = 2.59$ (dashed line in figure 13b). Initially, for both Reynolds numbers the shape factor shows a slight and constant increase trend up until a certain angle, $\theta \approx 70^{\circ}$. This zone corresponds with the favorable pressure gradient zone, where the flow in the boundary layer accelerates (see also figure 8 where the pressure coefficient along the sphere circumference is shown). Once the boundary layer enters the adverse pressure gradient zone and approaches separation, the shape factor rapidly increases. The separation of the boundary layer is eventually reached at $H \approx 4 - 4.5$. The location of the separation point for both Reynolds numbers is marked in the figure with a solid dot. Note also that the shape factor for the circular cylinder at subcritical Reynolds numbers [47] is also included in figure 13b for comparison. It is interesting to point out that the shape factor for both sphere and cylinder at sub-critical Reynolds numbers behaves similarly. In both cases,

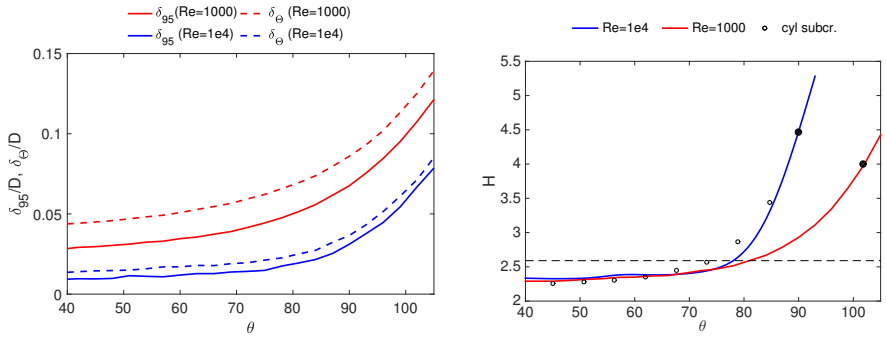

(a) (b)

Figure 13: Boundary layer integral quantities at $Re = 1000$ and $Re = 10^4$. (a) Viscous and thermal boundary layer thicknesses, (b) viscous boundary layer shape factor. (open circles) solution for the subcritical circular cylinder, (solid dots) location of the separation point, (black dashed line) Blasius solution shape factor.

in the sub-critical regime the minimum pressure gradient is attained at around $\theta = 70^\circ$ and separation occurs at $\theta \approx 90^\circ$. Thus, the zones where the boundary layer accelerates and enters the adverse pressure gradient are approximately the same.

3.4. Near wake mean and RMS temperature

The mean time-average temperature and its fluctuations in the near wake behind the sphere for both Reynolds numbers are plotted in figure 14, together with the turbulent kinetic energy contours. As was previously commented, the near wake exhibits a rapid mixing of the passive scalar as the irrotational fluid from the surroundings enters the wake. The results suggest that the temperature rapidly spreads out in the vortex formation zone, the temperature decrease being faster for the larger Reynolds number, i.e. $Re = 10^4$. Actually, at $Re = 10^4$ the turbulent kinetic energy in the wake is larger (see figure 14 e, f); this increase in the turbulent kinetic energy in the near wake induces a larger entrainment of fluid from outside the wake improving the mixing with colder fluid. As a consequence, the temperature in the wake decreases faster at $Re = 10^4$.

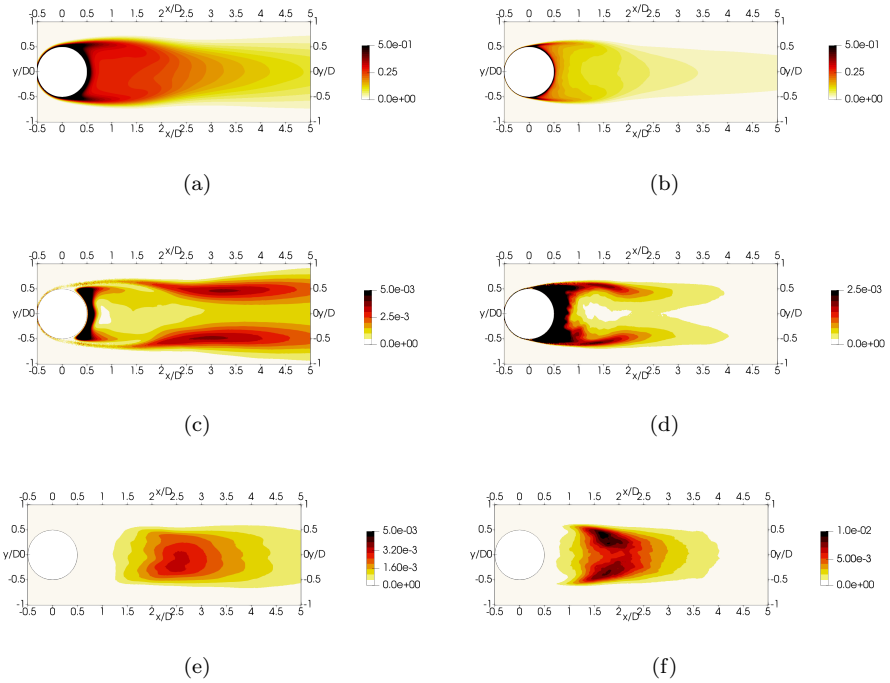

Figure 14: Temperature (a, b) and its fluctuations (c, d) together with turbulent kinetic energy (e,f) in the wake of the sphere (a,c,e) $Re = 1000$, (b,d,f) $Re = 10^4$.

In figure 15, the temperature Θ evolution along the wake centreline and its fluctuations Θ_{rms} are plotted for both Reynolds numbers. In the figure, the experimental data at $x/D = 14$ obtained by Freymuth and Uberoi [10] at $Re = 8300$ is also represented. Note the strong dependence with the Reynolds number of these variables. Actually, the wake at $Re = 8300$ and at $Re = 10^4$ can be considered mostly the same as at these Reynolds numbers the wake has evolved into the subcritical regime, but at $Re = 1000$ is still in transition from laminar to turbulent flow and exhibits a different behaviour. In fact, this different behaviour can also be quantified by evaluating the half-wake width $L_{v\,1/2}$. Here, it is defined as the distance between the wake axis and the radial location where the non-dimensional defect velocity equals $e^{-1/2}$, as in Legendre et al. [48]: $(U - u(x,r))/(U - u(x,0)) = e^{-1/2}$. In a similar manner, the scalar half-wake width $L_{\Theta\,1/2}$ has been defined as $\Theta(x,r)/\Theta(x,0) = e^{-1/2}$. It is important to remark, that in order to enforce the axisymmetry of the flow, at the different x/D locations when computing the wake width, radial velocity profiles are extracted at 24 polar angles equispaced between 0 and 2π. To extract these radial profiles, the unstructured data is projected using high order interpolations. After that, at each stream-wise location x/D, these equispaced radial profiles are averaged.

In figure 16 these values are given for both Reynolds numbers. Note the change in slope when the Reynolds number increases. Actually, at $Re = 1000$, the wake spreads as $L_{v\,1/2} \sim x/D^{0.526\pm0.009}$ and $L_{\Theta\,1/2} \sim x/D^{0.495\pm0.009}$ for the temperature up to $x/D = 15$, which are scalings close to the $x/D^{1/2}$ slope. This is in agreement with the faster decay observed by Wu & Faeth [4] in the near wake at these Reynolds numbers. After $x/D = 15$ the slope seems to decrease, although as this work focuses on the near wake between $5 \leqslant x/D \leqslant 15$, the accuracy of the present computations beyond $x/D = 15$ is not enough to confirm this change. At $Re = 10^4$, the wake width increases as $L_{v\,1/2} \sim x/D^{0.334\pm0.012}$ and $L_{\Theta\,1/2} \sim x/D^{0.346\pm0.007}$ for the temperature. These values are close to the $x/D^{1/3}$ slope and also in agreement with the observations of Wu & Faeth [4]. At the same Reynolds number, Stadler et al. [13] found a wake growth proportional

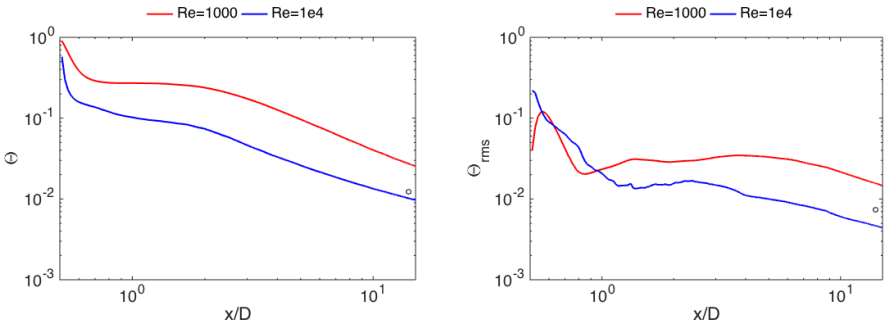

(a) (b)

Figure 15: (a) Temperature and (b) its fluctuations at the wake centreline for $Re = 1000$ and $Re = 10^4$. The open circle represents the experimental results by Freymuth&Uberoi[10] at $Re = 8300$.

to $x/D^{0.39}$, which is a value slightly larger than the 1/3 slope and $x^{0.44}$ for the temperature, closer to the non-equilibrium scaling proposed by Nedić et al. [12] and Obligado et al. [15]. Note that these non-equilibrium scalings were obtained for wake distances of $x/L_b = 10 - 50$, or $x/D = 10 - 35$ in the case of Stadler et al. [13], while the present study is focused on the near wake region, and the data further downstream might be insufficient to perform an accurate scaling.

4. Conclusions

High-fidelity numerical simulations of the fluid dynamics and heat transfer of the flow past a sphere at low-to-moderate Reynolds numbers of $Re = 1000$ and $Re = 10^4$ and $Pr = 0.7$ have been performed. In general, important differences in the fluid dynamics and heat transfer have been observed when the flow goes from $Re = 1000$ to $Re = 10^4$. These differences stem from the different regimes for the flow at $Re = 1000$ and $Re = 10^4$. In fact, at $Re = 1000$ the flow is in transition from laminar unsteady flow to a turbulent sub-critical regime where transition to turbulence seems to occur in the wake behind the sphere, whereas the flow at $Re = 10^4$ is in the sub-critical regime, where the

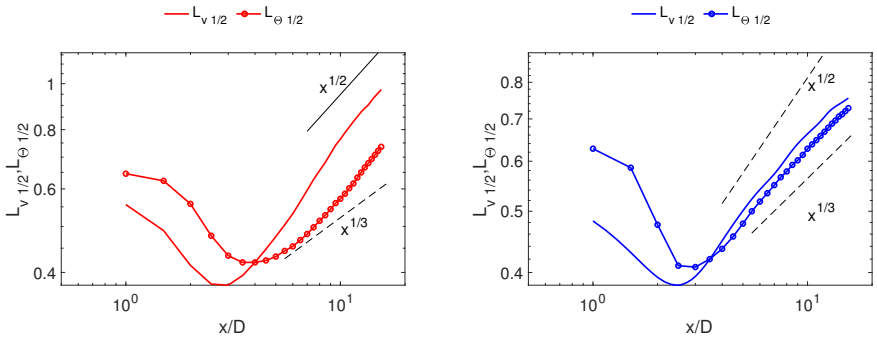

Figure 16: Half wake width for (a) $Re = 1000$ and (b) $Re = 10^4$.

boundary layer is laminar but transition to turbulence occurs in the separated shear layers. Differences in the flow parameters have been observed in both cases, with the separation point moving towards the sphere apex and the drag coefficient decreasing as the Reynolds number increases. These differences in the flow regime are also observed in the near wake flow dynamics where large fluctuations are observed for the largest Reynolds number.

The average and local Nusselt numbers have also been obtained. A fair agreement with experimental measurements has been observed. Small deviations with experimental data seem to be due to the influence of inlet turbulence and the sphere support on the measurements. Actually, the best agreement seems to be with experimental data extrapolated to a zero level of turbulence. Local Nusselt number reaches its maximum value in the front stagnation point to decrease up to a minimum value just after boundary layer separation. This minimum value is attained at $\theta = 114^\circ$ and $\theta = 95^\circ$ for $Re = 1000$ and $Re = 10^4$, respectively. These differences in the location of local Nusselt number minimum are also due to the different flow regimes observed.

The viscous and thermal boundary layers have been measured and as expected, the boundary layer thickness decreases with the Reynolds numbers, with the thermal boundary layer being slightly thicker than the viscous one. In

the zone with favourable pressure gradient, the shape factor of the boundary layer increases steadily but at a reduced rate, its value being lower than the one predicted by the Blausius solution for a laminar boundary layer. However, once the boundary layer enters the zone with adverse pressure gradient the value of the shape factor rapidly increases and separation is attained at $H \approx 4 - 4.5$, the largest value being for $Re = 10^4$.

The differences observed between both Reynolds numbers are also sustained by the behaviour of the near wake, where mixing increases the entrainment of irrotational flow in the recirculation zone and produces a faster decrease in the temperature for $Re = 10^4$. After the closure of the recirculation bubble, and in agreement with observations of Wu & Faeth [4], the near wake between $5 \leqslant x/D \leqslant 15$ spreads at a faster rate at $Re = 1000$ with a slope close to $x/D^{1/2}$, while at $Re = 10^4$ it follows a spread closer to $x/D^{1/3}$.

Acknowledgments

This work has been partially financially supported by the Ministerio de Economía y Competitividad, Secretaría de Estado de Investigación, Desarrollo e Innovación, Spain (refs. ESP2016-79612-C3-2-R & TRA2017-88508-R). We also acknowledge Red Española de Surpercomputación (RES) for awarding us access to the MareNostrum IV machine based in Barcelona, Spain (Ref. FI-2017-2-0012 & FI-2017-3-0018).

References

[1] E. Achenbach, Experiments on the flow past spheres at very high Reynolds numbers, Journal of Fluid Mechanics 54 (1972) 565–575.

[2] E. Achenbach, Vortex shedding from spheres, Journal of Fluid Mechanics 62 (2) (1974) 209–221.

[3] H. Kim, P. Durbin, Observations of the frequencies in a sphere wake and of drag increase by acoustic excitation, Physics of Fluids 31 (11) (1988) 3260–3265.

[4] J. S. Wu, G. M. Faeth, Sphere wakes in still surroundings at intermediate Reynolds numbers, AIAA Journal 31 (8) (1993) 1448–1455. doi:10.2514/3.11794.

[5] I. Rodríguez, R. Borrell, O. Lehmkuhl, C. D. Pérez-Segarra, A. Oliva, Direct numerical simulation of the flow over a sphere at Re = 3700, Journal of Fluid Mechanics 679 (2011) 263–287. doi:10.1017/jfm.2011.136.

[6] I. Rodríguez, O. Lehmkuhl, R. Borrell, A. Oliva, Flow dynamics in the wake of a sphere at sub-critical Reynolds numbers, Computers & Fluids 80 (2013) 233–243. doi:10.1016/j.compfluid.2012.03.009.

[7] Y. Bazilevs, J. Yan, M. de Stadler, S. Sarkar, Computation of the Flow Over a Sphere at Re=3700: A Comparison of Uniform and Turbulent Inflow Conditions, Journal of Applied Mechanics 81 (12) (2014) 121003. doi:10.1115/1.4028754.

[8] M. Dominguez-Pumar, M. Atienza, L. Kowalski, S. Novio, G. S., Heat flow dynamics in thermal systems described by diffusive representation, IEEE Transactions on Industrial Electronics 64 (1) (2017) 664–673.

[9] M. S. Uberoi, P. Freymuth, Turbulent Energy Balance and Spectra of the Axisymmetric Wake, Physics of Fluids 13 (9) (1970) 2205–2210. doi:10.1063/1.1693225.

[10] P. Freymuth, M. S. Uberoi, Temperature fluctuations in the turbulent wake behind an optically heated sphere, Physics of Fluids 16 (2) (1973) 161. doi:10.1063/1.1694309.

[11] P. Johansson, W. George, The far downstream evolution of the high-Reynolds-number axisymmetric wake behind a disk. Part 1. SIngle point statistics, Journal of Fluid Mechanics 555 (2006) 363–385. doi:10.1017/S0022112006009517.

[12] J. Nedić, J. C. Vassilicos, B. Ganapathisubramani, Axisymmetric turbulent wakes with new nonequilibrium similarity scalings, Physical Review Letters 111 (14) (2013) 1–5. doi:10.1103/PhysRevLett.111.144503.

[13] M. B. de Stadler, N. R. Rapaka, S. Sarkar, Large eddy simulation of the near to intermediate wake of a heated sphere at Re=10000, International Journal of Heat and Fluid Flow 49 (2014) 2–10. doi:10.1016/j.ijheatfluidflow.2014.05.013.

[14] T. Dairay, M. Obligado, J. C. Vassilicos, Non-equilibrium scaling laws in axisymmetric turbulent wakes, Journal of Fluid Mechanics 781 (2015) 166–195. doi:10.1017/jfm.2015.493.

[15] M. Obligado, T. Dairay, J. C. Vassilicos, Nonequilibrium scalings of turbulent wakes, Physical Review Fluids 1 (4) (2016) 044409. doi:10.1103/PhysRevFluids.1.044409.

[16] H. Kramers, Heat transfer from spheres to flowing media, Physica 12 (2) (1946) 61–80. doi:10.1016/S0031-8914(46)80024-7.

[17] T. Yuge, Experiments on Heat Transfer From Spheres Including Combined Natural and Forced Convection., Journal of Heat Transfer 82 (3) (1960) 214–220. doi:10.1115/1.3679912.

[18] G. C. Vliet, G. Leppert, Forced convection heat transfer from an isothermal sphere to water, Journal of Heat Transfer 83 (1961) 163. doi:10.1115/1.3680504.

[19] T. R. Galloway, B. H. Sage, thermal and material transfer in tubulent gas Streams-a Method of Prediction for Spheres, International Journal of Heat and Mass Transfer 7 (1964) 283–291.

[20] G. D. Raithby, E. R. G. Eckert, The effect of turbulence parameters and support position on the heat transfer from spheres, International Journal of Heat and Mass Transfer 11 (1968) 1233–1252.

[21] S. Whitaker, Forced Convection Heat Transfer Correlations for Flow In Pipes, Past Flat Plates, Single, AIChE Journal 18 (2) (1972) 361–371. doi:10.1002/aic.690180219.

[22] G. J. Kowalski, J. W. Mitchell, Heat transfer from spheres in the naturally turbulent, outdoor environment, The American Society of Mechanical Engineers 75-WA/HT-5 (4) (1975) 1–7. doi:10.1115/1.3450614.

[23] R. Kurose, M. Anami, A. Fujita, S. Komori, Numerical simulation of flow past a heated/cooled sphere, Journal of Fluid Mechanics 692 (2012) (2012) 332–346. doi:10.1017/jfm.2011.517.

[24] J. B. Will, N. P. Kruyt, C. H. Venner, An experimental study of forced convective heat transfer from smooth, solid spheres, International Journal of Heat and Mass Transfer 109 (2017) 1059–1067. doi:10.1016/j.ijheatmasstransfer.2017.02.018.

[25] W. W. Short, R. A. S. Brown, B. H. Sage, Thermal Transfer in Turbulent Gas Streams. Effect of Turbulence on Local Transport From Spheres, Journal of Applied Mechanics 27 (3) (1960) 393–402. doi:10.1115/1.3644014.

[26] K. Lee, H. Barrow, Transport processes in a flow around a sphere with particular reference to the transfer of mass, International Journal of Heat and Mass Transfer. 11 (1968) 1013–1026.

[27] L. Zhitkevich, L. Simchenko, Investigation of local and average heat transfer between a sphere and an airstream, Journal of Engineering Physics 11 (1) (1966) 10–14.

[28] T. R. Galloway, B. H. Sage, Local and Macroscopic Thermal Transport from a Sphere in a Turbulent Air Stream, AIChE Journal 18 (2) (1972) 287–293.

[29] G. L. Hayward, D. C. T. Pei, Local heat transfer from a single sphere to a turbulent air stream, International Journal of Heat and Mass Transfer 21 (1978) 35–41.

[30] P. Bagchi, M. Ha, S. Balachandar, Direct numerical simulation of flow and heat transfer from a sphere in a uniform cross-flow, Journal of Fluids Engineering 123 (2001) 347–358.

[31] L. Kowalski, M. T. Atienza, S. Gorreta, V. Jimenez, M. Dominguez-Pumar, S. Silvestre, L. M. Castañer, Spherical Wind Sensor for the Atmosphere of Mars, IEEE Sensors Journal 16 (7) (2016) 1887–1897. doi:10.1109/JSEN.2015.2509168.

[32] A. W. Vreman, An eddy-viscosity subgrid-scale model for turbulent shear flow: Algebraic theory and applications, Physics of Fluids 16 (10) (2004) 3670–3681. doi:10.1063/1.1785131.

[33] O. Lehmkuhl, G. Houzeaux, M. Avila, H. Owen, M. Vazquez, D. Mira, A low dissipation finite element scheme for the large eddy simulation on complex geometries, in: 19h International Conference on Finite Elements in Flow Problems - FEF 2017, 2017.

[34] F. Capuano, G. Coppola, L. Rández, L. de Luca, Explicit Runge-Kutta schemes for incompressible flow with improved energy-conservation properties, Journal of Computational Physics 328 (2017) 86–94.

[35] F. X. Trias, O. Lehmkuhl, A self-adaptive strategy for the time integration of Navier-Stokes equations, Numerical Heat Transfer. Part B 60 (2) (2011) 116–134. doi:10.1080/10407790.2011.594398.

[36] M. Vázquez, G. Houzeaux, S. Koric, A. Artigues, J. Aguado-Sierra, R. Arís, D. Mira, H. Calmet, F. Cucchietti, H. Owen, A. Taha, E. D. Burness, J. M. Cela, M. Valero, Alya: Multiphysics engineering simulation toward exascale, Journal of Computational Science 14 (2016) 15–27. doi:10.1016/j.jocs.2015.12.007.

[37] A. Tomboulides, S. Orszag, Numerical investigation of transitional and weak turbulent flow past a sphere, Journal of Fluids Mechanics 416 (2000) 45–73.

[38] H. Sakamoto, H. Haniu, A study on vortex sheding from spheres in an uniform flow, Journal of Fluids Engineering 112 (1990) 386–392.

[39] G. Constantinescu, M. Chapelet, K. Squires, Turbulence modeling applied to flow over a sphere, AIAA Journal 41 (9) (2003) 1733–1741.

[40] G. Yun, D. Kim, H. Choi, Vortical structures behind a sphere at subcritical Reynolds numbers, Physics of Fluids 18.

[41] H. Sakamoto, H. Haniu, The formation mechanism and shedding frequency of vortices from a sphere in uniform shear flow, Journal of Fluid Mechanics 287 (1995) 151–171.

[42] C. Wieselsberger, Further information on the laws of fluid resistance, Technical note (1922).

[43] J. Jeong, H. Fazle, On the identification of a vortex, Journal of Fluids Mechanics 285 (69–94). doi:10.1017/S0022112095000462.

[44] S. Pope, Turbulent Flows, Cambridge University Press, 2000.

[45] N. Frössling, Evaporation, heat transfer, and velocity distribution in two-dimensional and rotationally symmetrical laminar boundary layer flow , Tech. Rep. ,ADB189168, National Advisory Committee for Aeronautics (1956).

[46] V. Seidl, S. Muzaferija, M. Peric, Parallel DNS with local grid refinement, Applied Scientific Reseach 59 (1998) 379–394.

[47] W. Cheng, D. I. Pullin, R. Samtaney, W. Zhang, W. Gao, Large-eddy simulation of flow over a cylinder with from to : a skin-friction perspective, Journal of Fluid Mechanics 820 (2017) 121–158. doi:10.1017/jfm.2017.172.

[48] D. Legendre, A. Merle, J. Magnaudet, Wake of a spherical bubble or a solid sphere set fixed in a turbulent environment, Physics of Fluids 18 (4) (2006) 1–5. doi:10.1063/1.2191885.